Aust. Met. Mag. 45 (1996) 19–40

A numerical experiment on the Adelaide gully wind of South Australia

W. Sha
Department of Mechanical and Control Engineering
University of Electro-Communications, Japan
W. Grace
Regional Office, Bureau of Meteorology, Adelaide, Australia
and
W. Physick
CSIRO Division of Atmospheric Research, Australia

(Manuscript received March 1995; revised September 1995)

A three-dimensional, non-hydrostatic, terrain-following numerical model was used to investigate the Adelaide gully wind of South Australia. It reproduced most features of this downslope wind.
Results showed that the onset and strength of the Adelaide gully wind are critically dependent on the upstream wind and potential temperature profiles, and that the appearance of this local wind is also strongly influenced by the complicated three-dimensional effect of the real topography. The results also suggest that the production of the Adelaide gully wind can be explained by either the wave-resonant amplification mechanism or the hydraulic amplification mechanism.
A sensitivity study of the numerical model showed that a grid size of $\Delta x = \Delta y = 1$ km is desirable for resolving the fine structures of the Adelaide gully wind, including regions of reversed wind flow at the surface.

Introduction

Downslope winds have been observed in the lee of mountain ranges in all parts of the world. They include the foehn of alpine Europe (Hoinka 1985a), the bora of Yugoslavia (Smith 1987), the chinook of the Colorado Rocky Mountains (Lilly and Zipser 1972), yamaji-kaze of Japan (Akiyama 1956), the scarp wind of Perth (Pitts and Lyons 1989, 1990; Blockley and Lyons 1994) and Adelaide gully wind (Holton 1985; Marsh 1987; Grace and Holton 1988, 1990; Holton and Grace 1989a, b; Grace 1992, 1995). One of the most documented and most studied downslope winds is that of Boulder, Colorado (e.g. Brinkmann 1974; Klemp and Lilly 1975, 1978; Lilly 1978; Peltier and Clark 1979; Durran and Klemp 1983; Clark and Farley 1984; Hoinka 1985b; Bower and Durran 1986; Durran 1986; Neiman et al. 1988; Richard et al. 1989; Scinocca and Peltier 1989). Generally, features of strong downslope winds are a night-time speed enhancement, sudden onset, marked variability in strength but not in direction, and a stable layer or inversion near or just above hilltop level. The cross-section of the mountain range is usually ramp-shaped (i.e. gently sloping to windward with a much steeper slope to leeward), for which the wave amplitude and wave drag are significantly enhanced (Lilly and Klemp 1979; Miller and Durran 1991). In some areas, downslope winds may gust to more than 50 m/s, creating a hazard to aviation, in particular, and damage to buildings and trees.

Several explanations have been proposed for the development of strong downslope winds:

Corresponding author address: Dr W. Sha, Nagoya Institute of Technology, Gokiso-cho, Showa-ku, Nagoya 466, Japan.

Vol 45(1) Mar'96

firstly, an explanation based on analogy with hydraulic flow over an obstacle where there is a transition from subcritical to supercritical flow (for example, Kuttner (1939) and especially Long (1954)). Attractive as the hydraulic theory is, it has the disadvantage of not accounting for the vertical transport of energy of internal gravity waves. A second explanation (Klemp and Lilly 1975) is based upon the superposition of upward and downward propagating waves partially reflected at interfaces of changing Scorer parameter. This explanation of a nonlinear phenomenon based on a linear effect has not proved especially useful. A third explanation (Clark and Peltier 1977) is that wave breaking plays an important role. Vertically propagating waves become statically unstable and break, thereby creating a region of strong mixing and local wind reversal. This region, in turn, acts as a reflecting layer thereby trapping waves, which grow with time, ultimately producing very strong surface winds. A lucid and comprehensive review is provided by Durran (1990) although there is still lively discussion as to the relative merits of the first and third explanations.

Wave breaking of homogeneous flow over topography has been studied extensively with numerical models (Durran 1986; Laprise and Peltier 1989; Bacmeister and Schoeberl 1989; Ikawa and Nagasawa 1989; Ikawa 1990; Saito and Ikawa 1991; Miranda and James 1992; Saito 1993); a hydraulic model (Baines and Granek 1990) and water tank apparatus (Castro et al. 1983; Baines and Hoinka 1985; Castro 1987; Rottman and Smith 1989). These works show that a severe wind state can develop even when the mean wind speed and the stability are uniform with height, as long as there is a wave-breaking region aloft acting as a wave-induced critical layer. This hypothesis was explored further by Clark and Peltier (1984), Tomine (1984, 1987), Durran and Klemp (1987), Klemp and Durran (1987), Bacmeister and Pierrehumbert (1988), Pitts and Lyons (1990) and Scinocca and Peltier (1991), who simulated the evolution of mountain waves propagating in an ambient flow that had a pre-existing zero-wind line referred to as an 'enviromental critical level'. Durran and Klemp (1987) and Bacmeister and Pierrehumbert (1988) discussed the dependence of the high-drag state solution on the mountain height and the critical-level elevation. They showed that the character of the severe wind state conforms closely to the predictions of the nonlinear analytic solutions of Smith's internal hydraulic theory (Smith 1985) and to a similar theory by Grace (1992, 1995). Scinocca and Peltier (1991) found that the temporal evolution of the flow towards the high-drag state is also strongly influenced by the value of local gradient Richardson number, Ri to a degree that depends on the strength of the topographic forcing. For severe downslope windstorms, this dynamical instability may represent a strong source of turbulence through a release of the instability on the lee slope of the mountain (Clark and Farley 1984; Scinocca and Peltier 1989, 1993, 1994; Peltier and Scinocca 1990; Smith 1991). Recently, more and more results suggest that the wave-breaking mechanism, which amplifies the drag and the downslope wind, is fundamentally similar to that produced through the transition from subcritical flow to supercritical flow in shallow-water hydraulic theory. In this view, the current, which develops beneath the breaking region, closely resembles an internal hydraulic jump (Clark and Peltier 1984; Durran 1986; Durran and Klemp 1987; Klemp and Durran 1987; Bacmeister and Pierrehumbert 1988; Pitts and Lyons 1990; Ikawa and Nagasawa 1989; Ikawa 1990; Saito and Ikawa 1991; Saito 1993).

Holton (1985) conjectured a hydraulic-jump mechanism for the Adelaide gully wind based upon its association with strong stability in the lower levels up to 500–1000 m. An additional mechanism applicable to the Adelaide gully wind proposed by Grace and Holton (1990) and modelled by Grace (1995) assumes that a cool, shallow air mass, usually in the form of a sea-breeze, moves inland during the day to the eastern side of the Mt Lofty Ranges (see Fig. 1). This air mass is then inertially trapped against the eastern flank of the ranges and builds to sufficient height to cascade down the western slopes as a gravity current, especially through the saddles and gullies. However, this mechanism is not associated with the strongest gully wind events.

In this study, we use a three-dimensional, nonhydrostatic, terrain-following mesoscale numerical model with an appropriate turbulence scheme to simulate the Adelaide gully wind of South Australia. The main purposes are (a) to identify causal mechanisms, (b) to determine under what synoptic upstream conditions the Adelaide gully wind occurs, and (c) to answer questions such as: how extensive is the Adelaide gully wind? how far to the lee does it blow? where is the position of the hydraulic jump and what is the spatial variation of the jump?

The organisation of this paper is as follows. The geographical features of the Mt Lofty Ranges and the climatological feature of the Adelaide gully wind are outlined followed by a description of the numerical model and the design of the numerical experiments. Next, the results for numerical experiments in which either the critical layer or the inversion layer is removed are shown, and the sensitivity to numerical horizontal resolution is also being investigated. Finally, a summary and outlook are given.

Fig. 1 Map of Mt Lofty Ranges. The rectangle framed by a solid line is the horizontal domain for the three-dimensional numerical experiments.

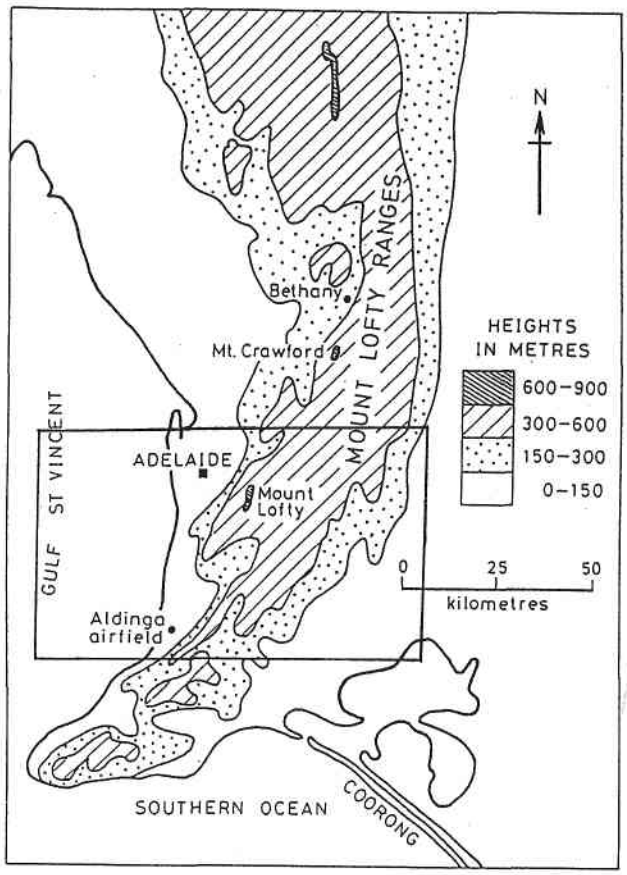

Geography of the Mt Lofty Ranges and observed features of the Adelaide gully wind

The Mt Lofty Ranges of South Australia (Fig. 1) are 40 to 50 km wide with an average height of the ridges of 500 m. The ranges have a ramp shape and are oriented approximately from north-northeast to south-southwest. To the west, the land falls steeply over a horizontal distance of 3 to 5 km, but then slopes gently across a coastal plain of varying width. The city of Adelaide is situated on this coastal plain.

Easterly downslope winds commonly occur on the western flank of the Mt Lofty Ranges and often extend several kilometres further westward. In the Adelaide region, the downslope winds are known as gully winds, for these winds are most pronounced over locally steeper lee slopes and gully sites. A common observation is of moderate easterly winds at the mountain tops with strong gusty easterly winds about the lee foothills, while a few kilometres further downstream the wind is light and may even be weakly reversed. Marsh (1987) reported a gust of 30 m/s at a wind-energy monitoring site that is located about 40 km south of Adelaide. Nineteen out of thirty gully-wind events, studied by Grace and Holton (1988), were associated with moderate to severe turbulence as reported by aircraft operating out of Adelaide Airport. In extreme cases, trees have been uprooted and houses have been damaged. The winds may also seriously hamper fire-fighting operations in the Mt Lofty Ranges.

Adelaide gully-wind events occur in the warmer months of November to March and during the night. Typically, they occur if the stream is a stable and vigorous east to southeasterly. Marsh (1987) identified a common synoptic situation for the damage-causing events; namely, a high centred at 40°S between 125° and 140°E, with a cold front moving across the east of Tasmania and extending a weak northern portion into the south-east of South Australia. An example is given in Fig. 2, which shows the synoptic situation at 0900 CST on 14 February 1980. Grace and Holton (1988, 1990) showed that the gully winds often had an easily identified onset and cessation. Namely, the wind regime switched sharply from light and variable to fast and fairly steady in direction, or vice versa. Analysing low-level winds from Adelaide Airport, Grace and Holton (1988) showed that there is typically a low-level jet at about 300 to 400 m associated with gully-wind events. About half the events had westerly 1000 m winds, and about a quarter had westerly or light winds at 600 m. Usually the wind above 1500–2000 m on a synoptic scale is westerly. These

Fig. 2 Mean sea-level pressure chart for 0900 CST 14 February 1980; typical for strong gully winds. Mark indicates the location of Adelaide city.

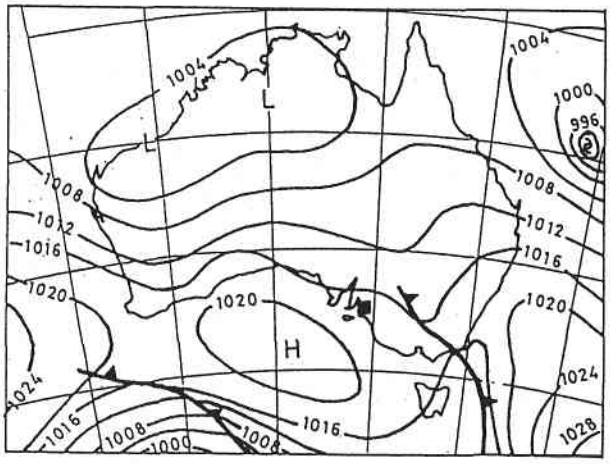

results emphasise the shallow nature of the gully winds. Contrary to conventional expectation, Grace and Holton (1988) also found that the presence of an elevated subsidence inversion on the Adelaide Airport sounding was a poor indicator of a subsequent or simultaneous gully-wind. Nonetheless, the most damaging gully-wind events do appear to be associated with a marked subsidence inversion or a post-frontal inversion. Isentropic analyses of a moderate gully-wind event by Grace (1992) at Fig. 3 show a decoupling of the flow above and below the 26°C isentrope originating upstream at about 1000 m altitude. Humidity cross-sections at Fig. 4 also reinforce this conclusion. The available upper winds above 1000 m are either very light or westerly. The overall impression is of striking similarity to a hydraulic jump.

Numerical model

Model equations

The model equations are based on the atmospheric primitive equations simplified by the anelastic and Boussinesq approximations. The

Fig. 3 Three-hourly isentropic cross-section for 2/3 February 1988 along bearing through Mt Lofty. Faint lines show aircraft and balloon trajectories. Offset winds are for Adelaide Airport and Nairne. Times are CST. (From Grace 1992.)

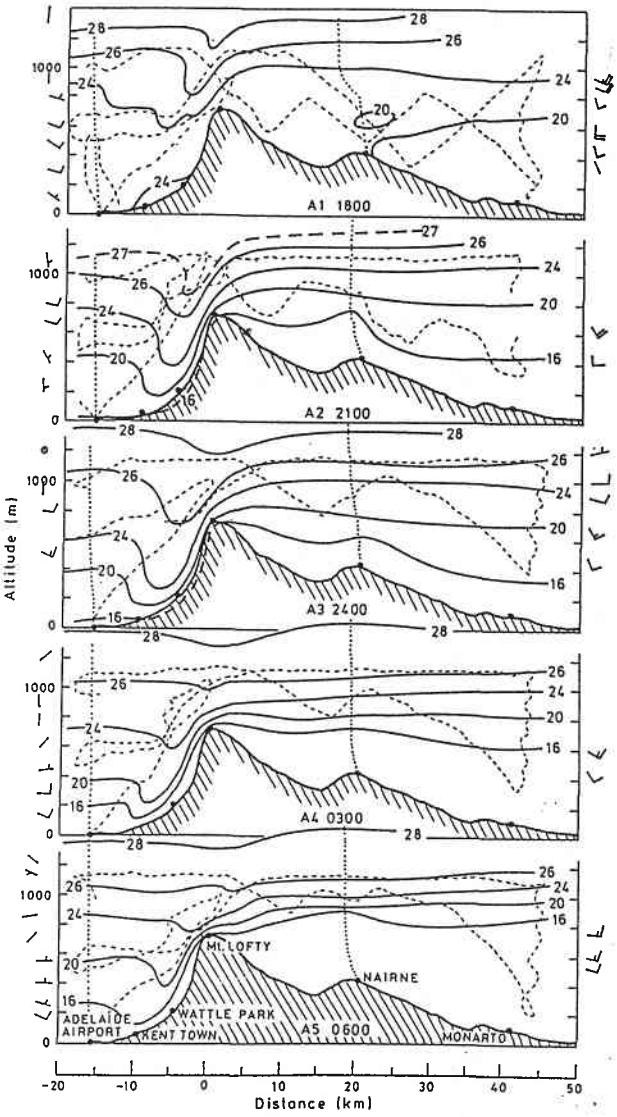

Fig. 4 As for Fig. 3 but specific humidity in g/kg. (From Grace 1992.)

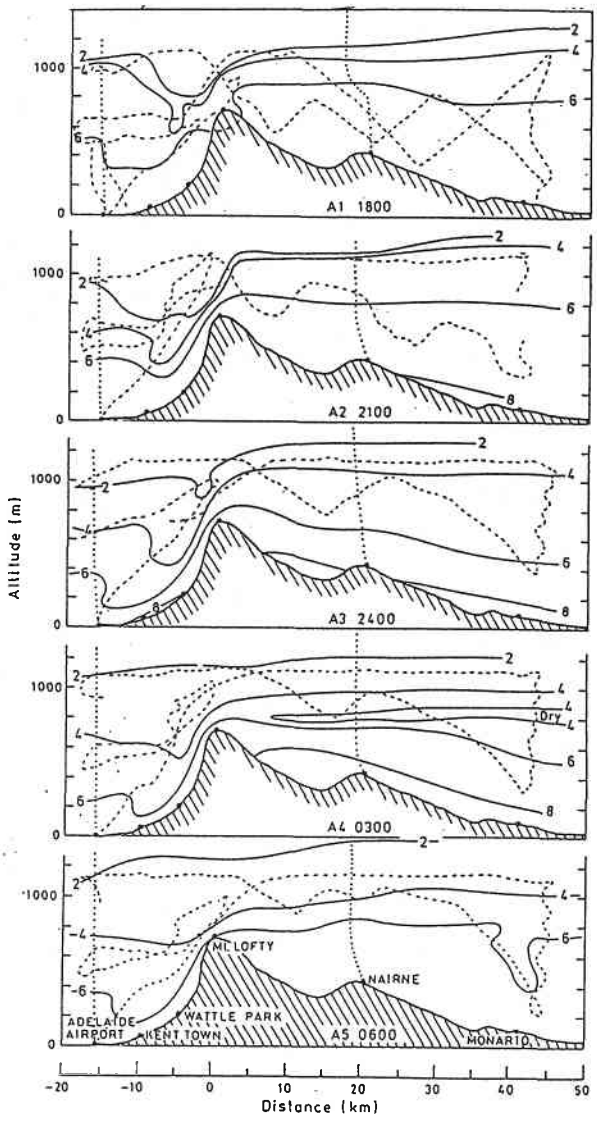

equations are averaged following Reynold's concept and the resulting covariances are parametrised by flux-gradient relations. For simulations of the air flow over topography, a terrain-following coordinate system is used. After transformation from the usual Cartesian coordinate (x, y, z) to the terrain-following coordinate (x, y, η) with

$$\eta = \frac{z-h}{H-h} \qquad \ldots 1$$

where $h(x, y)$ is the height of the topography and H is the height of model domain, the governing equations for a three-dimensional, non-hydrostatic and dry numerical model are

$$\frac{du}{dt} = f(v-v_g) - \frac{1}{\bar{\rho}}\frac{\partial p'}{\partial x} - \frac{1}{\bar{\rho}}\frac{\eta-1}{H-h}\frac{\partial h}{\partial x}\frac{\partial p'}{\partial \eta} + \frac{\partial}{\partial x}\left(K_{hm}\frac{\partial u}{\partial x}\right) + \frac{\partial}{\partial y}\left(K_{hm}\frac{\partial u}{\partial y}\right) + \frac{1}{(H-h)^2}\frac{\partial}{\partial \eta}\left(K_{vm}\frac{\partial u}{\partial \eta}\right) \qquad \ldots 2$$

$$\frac{dv}{dt} = -f(u-u_g) - \frac{1}{\bar{\rho}}\frac{\partial p'}{\partial y} - \frac{1}{\bar{\rho}}\frac{\eta-1}{H-h}\frac{\partial h}{\partial y}\frac{\partial p'}{\partial \eta} + \frac{\partial}{\partial x}\left(K_{hm}\frac{\partial v}{\partial x}\right) + \frac{\partial}{\partial y}\left(K_{hm}\frac{\partial v}{\partial y}\right) + \frac{1}{(H-h)^2}\frac{\partial}{\partial \eta}\left(K_{vm}\frac{\partial v}{\partial \eta}\right) \qquad \ldots 3$$

$$\frac{dw}{dt} = -\frac{1}{\bar{\rho}}\frac{\eta-1}{H-h}\frac{\partial p'}{\partial \eta} + \frac{\theta'}{\bar{\theta}}g + \frac{1}{H-h}\frac{\partial}{\partial x}\left(K_{vm}\frac{\partial u}{\eta}\right) + \frac{1}{H-h}\frac{\partial}{\partial y}\left(K_{vm}\frac{\partial v}{\eta}\right) \qquad \ldots 4$$

$$\frac{d\theta}{dt} = \frac{\partial}{\partial x}\left(K_{hh}\frac{\partial \theta}{\partial x}\right) + \frac{\partial}{\partial}\left(K_{hh}\frac{\partial \theta}{\partial y}\right) + \frac{1}{(H-h)^2}\frac{\partial}{\partial \eta}\left(K_{vh}\frac{\partial \theta}{\partial \eta}\right) \qquad \ldots 5$$

$$\frac{\partial}{\partial x}\left\{\bar{\rho}(H-h)u\right\} + \frac{\partial}{\partial y}\left\{\bar{\rho}(H-h)v\right\} + \frac{\partial}{\partial \eta}\left\{\bar{\rho}(H-h)\omega\right\} = 0 \qquad \ldots 6$$

where

$$\frac{d}{dt} = \frac{\partial}{\partial t} + u\frac{\partial}{\partial x} + v\frac{\partial}{\partial y} + \omega\frac{\partial}{\partial \eta} \qquad \ldots 7$$

The relationship between the vertical velocity w in the Cartesian coordinate system and that in the terrain-following system is given by

$$w = (H-h)\omega + (1-\eta)\left(u\frac{\partial h}{\partial x} + v\frac{\partial h}{\partial y}\right) \qquad \ldots 8$$

Besides the usual symbols in the aforementioned equations, p' and θ' are the mesoscale deviations of pressure and potential temperature from the basic state.

The turbulent eddy diffusivity for momentum K_{vm} is evaluated from the turbulent kinetic energy E and the turbulent dissipation rate ε. Transport equations for E and ε are as follows:

$$\frac{dE}{dt} = \frac{K_{vm}}{(H-h)^2}\left\{\left(\frac{\partial u}{\partial \eta}\right)^2 + \left(\frac{\partial v}{\partial \eta}\right)^2\right\} - \frac{K_{vh}}{H-h}\frac{g}{\bar{\theta}}\frac{\partial \theta}{\partial \eta} - \varepsilon + \frac{\partial}{\partial x}\left(\frac{k_{hm}}{\sigma_E}\frac{\partial E}{\partial x}\right) + \frac{\partial}{\partial y}\left(\frac{K_{hm}}{\sigma_E}\frac{\partial E}{\partial y}\right) + \frac{\partial}{\partial x}\left(\frac{K_{hm}}{\sigma_\varepsilon}\frac{\partial E}{\partial x}\right) + \frac{\partial}{\partial y}\left(\frac{K_{hm}}{\sigma_\varepsilon}\frac{\partial E}{\partial y}\right) \qquad \ldots 9$$

$$\frac{d\varepsilon}{dt} = c_{1\varepsilon}\frac{\varepsilon}{E}\left\{\frac{K_{vm}}{(H-h)^2}\left[\left(\frac{\partial u}{\partial \eta}\right)^2 + \left(\frac{\partial v}{\partial \eta}\right)^2\right] - (1-c_{3\varepsilon})\frac{g}{\bar{\theta}}\frac{K_{vh}}{H-h}\frac{\partial \theta}{\partial \eta}\right\} - c_{2\varepsilon}\frac{\varepsilon^2}{E} + \frac{\partial}{\partial x}\left(\frac{K_{hm}}{\sigma_\varepsilon}\frac{\partial \varepsilon}{\partial x}\right) + \frac{\partial}{\partial y}\left(\frac{K_{hm}}{\sigma_\varepsilon}\frac{\partial \varepsilon}{\partial y}\right) + \frac{1}{(H-h)^2}\frac{\partial}{\partial \eta}\left(\frac{K_{vm}}{\sigma_\varepsilon}\frac{\partial \varepsilon}{\partial \eta}\right) \qquad \ldots 10$$

where σ_E and σ_ε are the ratios of the eddy diffusivity for momentum to the turbulent kinetic energy and its dissipation rate, respectively. The vertical eddy diffusivity K_{vm} is then determined from the turbulent kinetic energy E and its dissipation rate ε as

$$K_{vm} = c_\mu\frac{E^2}{\varepsilon}, \qquad \ldots 11$$

in which both E and ε are solutions of Eqns 9 and 10. The vertical eddy diffusivity for heat, K_{vh}, is represented by

$$K_{vh} = \frac{K_{vm}}{\sigma_T} \qquad \ldots 12$$

where σ_T is the turbulent Prandtl number. All the constant values of the model parameters ($c_{1\varepsilon}$, $c_{2\varepsilon}$, $c_{3\varepsilon}$, c_μ) in Eqns 9 to 12 are the same as those used in a previous study (Sha et al. 1991). The horizontal eddy diffusivity for momentum, K_{hm}, in a nonlinear three-dimensional form (Pielke 1974a, 1974b; Mahrer and Pielke 1977; Physick 1988) defined as

$$K_{hm} = \beta(\Delta x\Delta y)\left\{\tfrac{1}{2}\left[\frac{\partial v}{\partial x} + \frac{\partial u}{\partial y}\right]^2 + \left[\frac{\partial u}{\partial x} + \frac{\partial v}{\partial y}\right]^2\right\}^{1/2} \qquad \ldots 13$$

was used, where β is a constant determined by numerical experiment and Δx and Δy are the grid spacings.

Surface heat energy balance

The surface temperature T_g, is determined by solving an energy budget equation at the earth's surface. Currently T_g is computed from

$$R_S + R_L = Q_H + Q_B \qquad \ldots 14$$

where R_S is the incoming flux of the solar radiation, R_L the outgoing long wave radiation flux, Q_H the sensible heat flux and Q_B the soil heat flux.

The calculations of the short wave radiative flux, R_S, and the long wave radiative flux, R_L, follow Gross (1987). The effect of terrain on the radiation components is taken into account. The heat fluxes Q_H and Q_B are given by

$$Q_H = -\bar{\rho} c_p u_* \theta_*,$$
$$Q_B = -\lambda_s \frac{\partial T_s}{\partial z_s} \qquad \ldots 15$$

where u_* is the friction velocity, θ_* the potential temperature scale, λ_s soil diffusivity, T_* soil temperature, and z_* denotes depth below the ground. Temperature in the soil is obtained from the heat conduction equation for which boundary conditions are the surface temperature and the soil constant temperature 0.5 m below the earth's surface.

Numerical aspects and computational domain

The prognostic equations presented in the section on model equations are integrated forward explicity in time with the time step chosen to satisfy the Courant-Friedrichs-Leury (CFL) criterion. Centred difference approximations are used in space; the advective terms are evaluated by upstream difference with a spline technique.

To increase the accuracy of the finite difference approximations, a staggered grid is used, both horizontally and vertically. In the horizontal directions, a grid interval of $\Delta x = \Delta y = 1000$ m is adopted, while in the vertical direction an expanding grid, with the greater resolution $\Delta Z = 20$ m near the ground, is used. Numerical calculation is performed on a $101 \times 61 \times 43$ grid-point domain while the top boundary is located at $z = 7.4$ km. An additional five levels are below the earth's surface to calculate heat flux in the soil.

The mesoscale pressure, p', is computed by solving a three-dimensional discrete Poisson equation with a Neumann boundary condition. The equation is solved directly by Gaussian elimination in the vertical and eigenfunction decomposition and fast Fourier transforms in the horizontal directions (Schumann and Volkert 1984).

Boundary and initial conditions

A no-slip lower boundary condition $u = v = 0$ is imposed. The land temperature, T_g, is obtained by solving the heat energy balance equation at the ground. For the turbulent kinetic energy, E, and its dissipation rate, ε, the boundary values are prescribed at the first grid level above the surface as

$$\varepsilon = \frac{u_*^3}{\kappa(\phi_m/z - 1/L)}$$
$$E = \left(\frac{\kappa u_* z \varepsilon}{\phi_m c_\mu}\right)^{1/2} \qquad \ldots 16$$

where κ is the Von-Karman constant, L the Monin-Obukhov length, and ϕ_m the universal function for momentum (Sha et al. 1991). At the upper boundary all variables are fixed at their initial values. In the upper levels of the model, an absorbing layer is employed using Rayleigh damping to suppress downward reflection of energy. At the inflow lateral boundary, u,v,w are fixed at their initial values and a similar absorbing region is installed upstream. This region serves to maintain the integrity of the upstream profiles throughout the integration. At the outflow lateral boundaries, a radiation condition is used (Sha et al. 1991). For potential temperature, θ, turbulent kinetic energy, E, and its dissipation, ε, at the lateral boundaries, it is assumed that

$$\frac{\partial}{\partial x}(\theta, E\ \varepsilon) = 0,$$
$$\frac{\partial}{\partial y}(\theta, E, \varepsilon) = 0. \qquad \ldots 17$$

Initial upwind profiles of velocity and potential temperature used in our experiments are designed to incorporate various characteristics of profiles observed in the Adelaide Hills region, but no particular case is modelled. These vertical profiles are assumed to be horizontally homogeneous in the computational domain. Based on the observed behaviour, the following numerical experiments are designed to investigate the sensitivity of the results to the upper-level westerly wind, the critical level and the elevated subsidence inversion.

Results and discussions

Control run with critical layer and elevated inversion layer

The initial velocity, u, and potential temperature profiles, θ, for the control run are shown in Fig. 5 (initial values of v and w are always set to zero).

Fig. 5 Initial velocity and potential temperature profiles for the control run.

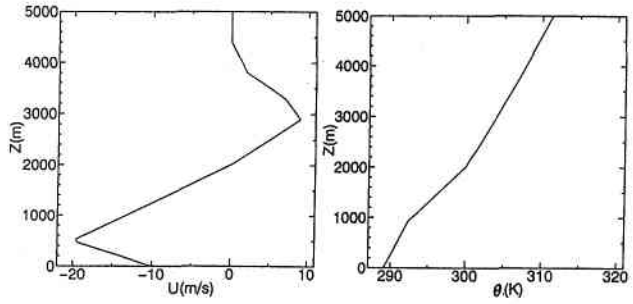

The easterly wind in the lower layer has a maximum value at 500 m, and then decreases linearly with height. The critical level ($u=0$) is set at 2000 m. Above the critical level, the wind blows westerly with a maximum at 3000 m, and above 4500 m winds are zero. An elevated inversion layer is specified in the layer 1000–2000 m above the ground.

The simulations were run until the numerical solutions achieved a quasi-equilibrium state. Figure 6 shows the horizontal winds at different altitudes. Strong surface winds are concentrated on the lee slope of the ranges. In the vicinity of Adelaide the strong winds extend down to the lee slope from the crest for about 4–5 km but then decrease rapidly to a minimum (8–19 km from the crest), and a reversed flow is formed. Further leeward the wind speed increases again. These results are in general agreement with the observations (Marsh 1987; Grace and Holton 1990). It is also seen in surface winds that the flow, beyond the urban area, has a wake-like pattern. This structure is considered to be associated with the reversed flow. On the other hand, the winds over the south part of the domain are much less changed. The reversed flow also coincides with rotor activity. At 200 m height, the wind pattern is similar to that of the surface, but the reversed flow is replaced by a minimum wind speed. At higher levels, the wind maximum moves upstream. At 740 m the wind becomes quite uniform except for the flow over the Mt Lofty summit. Thus, the shallow nature of the Adelaide gully winds is also reproduced by the model.

Figure 7 shows the vertical cross-sections of the wind vectors (u-w), horizontal velocity, u, potential temperature, θ, and gradient Richardson number, Ri, at $y=40$ km. In Fig.7 (a)–(b), strong downslope winds are developed on the lee side of the ranges and a wind speed maximum is formed just over the leeward slope. A stagnant tongue of fluid protrudes from the critical level. A region of reversed flow (a rotor) is formed above the hilltop at 1500 to 2000 m height, and the internal gravity waves are overturning. Separation occurs in the lower layer and then a shallow reversed circulation at the lee foothill is formed. Figure 7(c) illustrates the contours of the potential temperature. Wave breaking occurs within a trough about 8–10 km wide and is characterised by strong mixing and a local reversal of the wind. Above the 2000 m level, the vertically propagating internal gravity wave is suppressed. This feature can be understood from Fig. 7(d). Above 2000 m height, the Ri number is large ($Ri > 1.5$) whilst Kelvin-Helmholtz instability (KHI), indicated by slant lines, occurs inside the wave-breaking region. The wave-breaking region is acting as a reflector of the internal gravity waves. Thus, a resonance is established in the cavity between the ground and the reversed flow that in turns leads to the strong downslope wind on the lee slope. Vertical cross-sections of wind vectors, horizontal velocity, u, potential temperature, θ, and Ri at $y=10$ km are shown in Fig. 8. No severe downslope wind occurs. Compared with Fig. 7, the wave is not breaking although some waves are trapped in higher levels. The flow is passing over the range smoothly. The region of Kelvin-Helmholtz instability (KHI) does not exist. The surface wind speed across this section is relatively unchanged (see in Fig. 6)

Influence of the critical layer

The influence of the critical layer on the Adelaide gully winds was investigated by altering the upstream wind profile: (a) the critical level is retained while the westerly wind in the upper layer is removed, (b) the critical layer is replaced by a uniform wind above 500 m, (c) the critical layer is removed by specifying a uniform wind at all levels. In all experiments above, the upstream vertical potential temperature profile is the same as that of the control run. The horizontal wind, u, and potential temperature, θ, for these runs are displayed in Fig. 9.

Figures 10, 11 and 12 show the simulation results. Comparing the flow structures to the control run in Figs 6 and 7, we first see that the flow pattern in case (a) is almost the same as that of the control run. This suggests that the westerly wind in the upper layer is not a factor in generating the Adelaide gully wind. In two other cases, the numerical solutions are considerably different from that in the control run. Shooting flow appears along the lee slope and surface winds are enhanced on the lee slope, but they are weaker than that of the control case, and no wave breaking occurs. For each case the flow regime over the range appears analogous to a propagating hydraulic jump in the lower layer while in the upper layer the solution is dominated by a single

Fig. 6 Horizontal winds at different levels. The contour interval for topography is 100 m. (a) Wind vectors at surface (20 m), 200, 400 and 740 m, respectively. (b) Same as (a) but for contours of horizontal velocity u. The contour interval is 1 m/s.

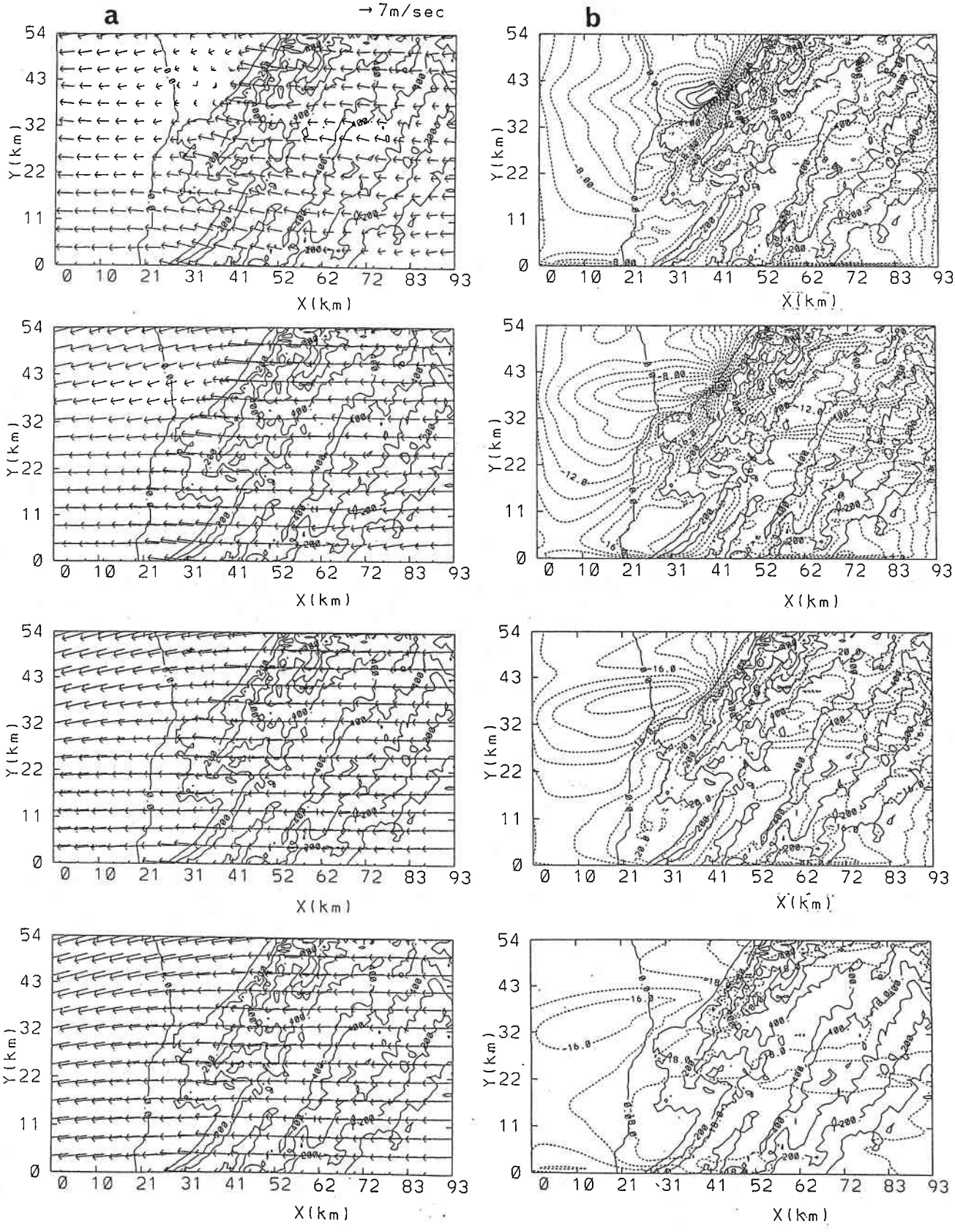

Fig. 7 (a) Vertical cross-section of wind vectors (u–w) at y = 40 km. (b) Vertical cross-section of the horizontal velocity u. The contour interval is 1 m/s. (c) As in (b) except for the potential temperature. The contour interval is 1 K. (d) As in (b) except for the Ri number. The contour interval is 0.25.

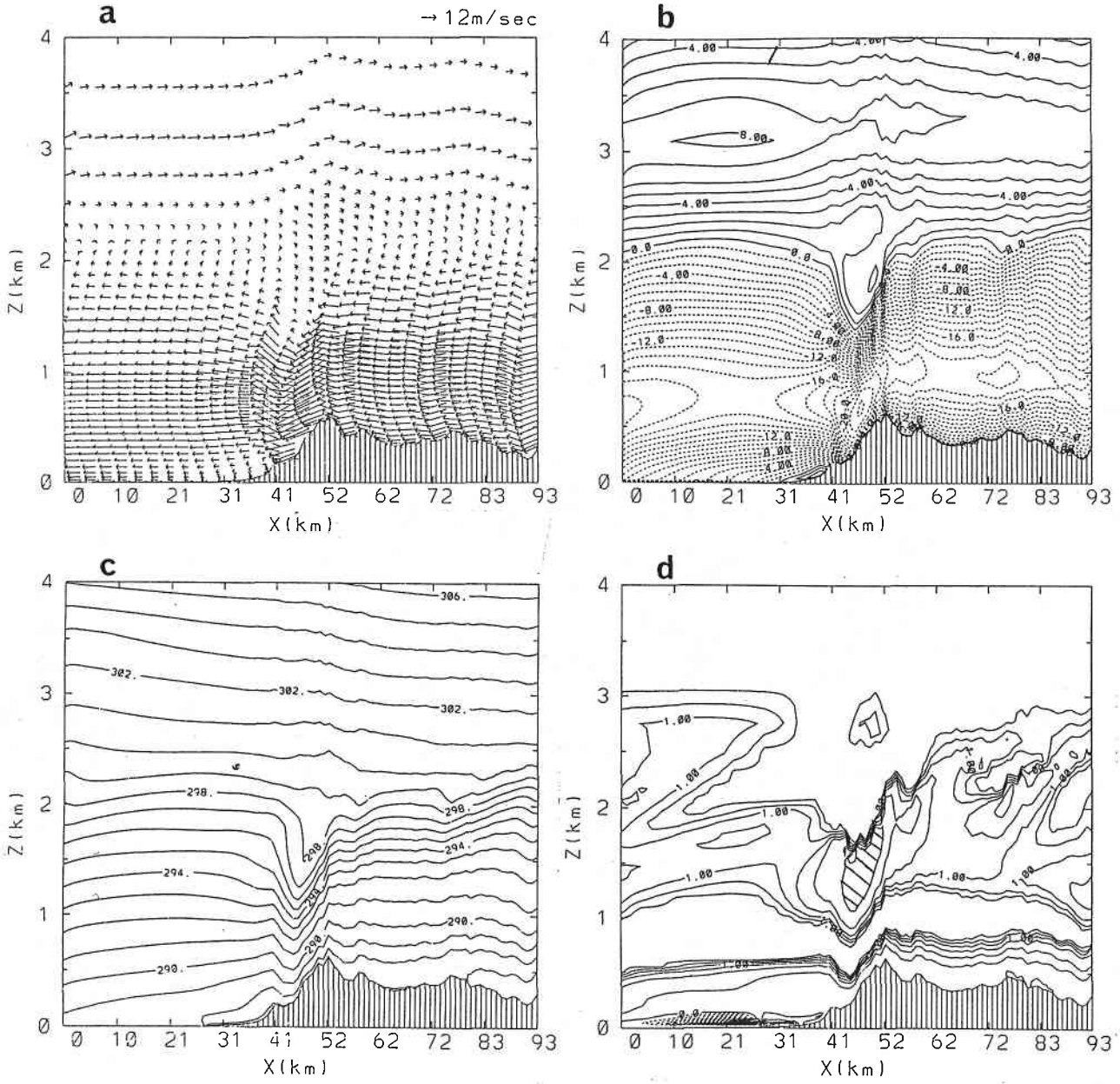

vertically propagating wave. It is demonstrated in the next section that the elevated inversion layer contributes to intensifying the surface wind speed in these hydraulic flows.

Influence of the elevated inversion layer

Figure 13 gives the initial upstream velocity, u, and the potential temperature, θ, in (a) which is the same as the control run but the elevated inversion layer is removed, (b) which is the same as that in Fig. 9(b) but without the elevated inversion, and (c) which is the same as that in Fig. 9(c) but without the elevated inversion layer. The numerical results are shown in Figs 14, 15 and 16, respectively. From Figs 14(a), 15(a) and 16(a), it is seen that the flow structure in case (a) is again very similar to the control run. It is concluded that an inversion layer is not necessary for the formation of a severe downslope wind whenever there is a pre-existing critical layer. However, the absence of the inversion layer does not appear to decrease the maximum wind speed in comparison to the previous section (b) and (c).

Fig. 8 As in Fig. 7 except for the cross-section at y = 10 km.

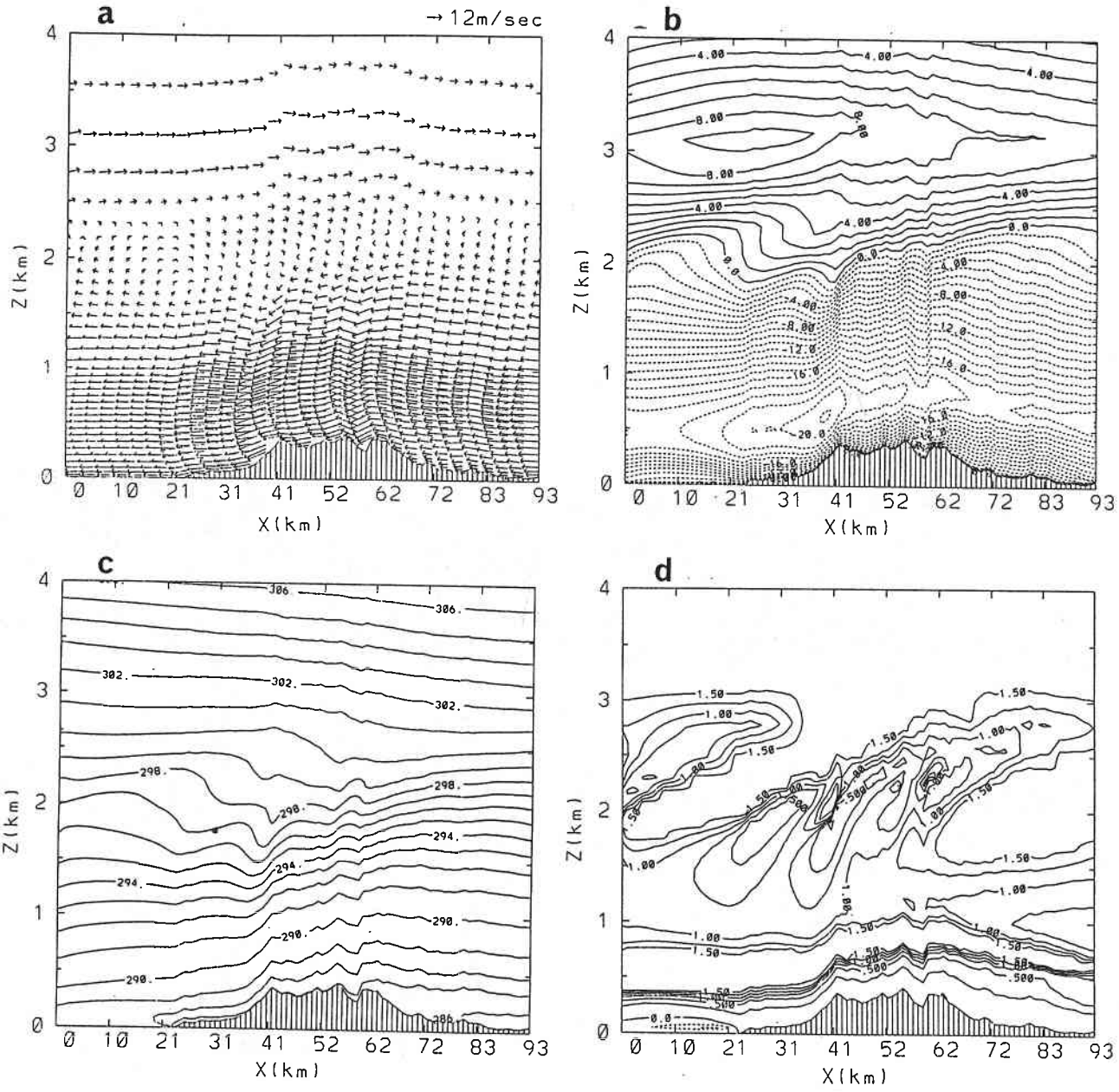

Sensitivity to horizontal grid spacing

To investigate the sensitivity of the numerical solutions to the horizontal grid spacing, the grid size was increased from 1 km to 2.5 km ($\Delta x = \Delta y = 2.5$ km). The number of the grid-points is $61 \times 61 \times 43$ and this extends the domain to 152.5×152.5 km. The upstream initial conditions are the same as in the control run. Figures 17 and 18 show the simulation results. Compared with Figs 6 and 7, the flow pattern is similar. However, it is found that fine structures such as the reversed flow are not reproduced with the coarser grid. In this run, the surface flow seems to go around the range rather than over it.

Summary and outlook

A three-dimensional, non-hydrostatic, terrain-following numerical model was used to investigate the Adelaide gully wind of South Australia, and it was found to reproduce this downslope wind quite well. The simulations show that onset and strength of this local wind is critically dependent on the upstream wind and potential temperature profiles and the topographic height. This is similar to the scarp wind at Perth (Pitts and Lyons 1990). The appearance of the Adelaide gully wind is also strongly influenced by the complicated three-dimensional effect of the real topography.

Fig. 9 As in Fig. 5 but for runs in the section on the influence at the critical layer.

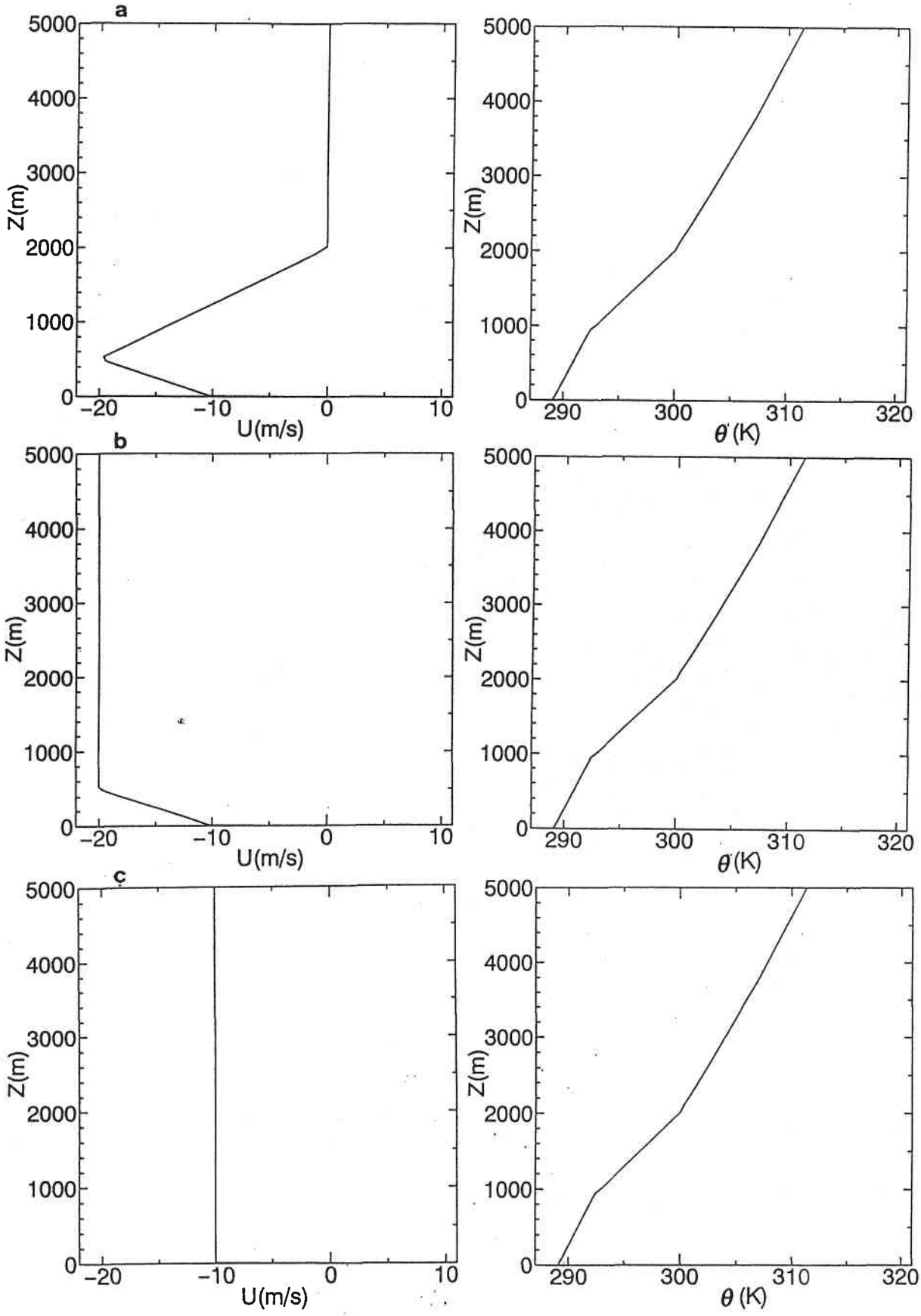

Fig. 10 **Horizontal winds at surface (20 m) for runs in the section on the influence of the critical layer. (a), (b) and (c). Wind vectors and horizontal velocity u for case a, b and c, respectively.**

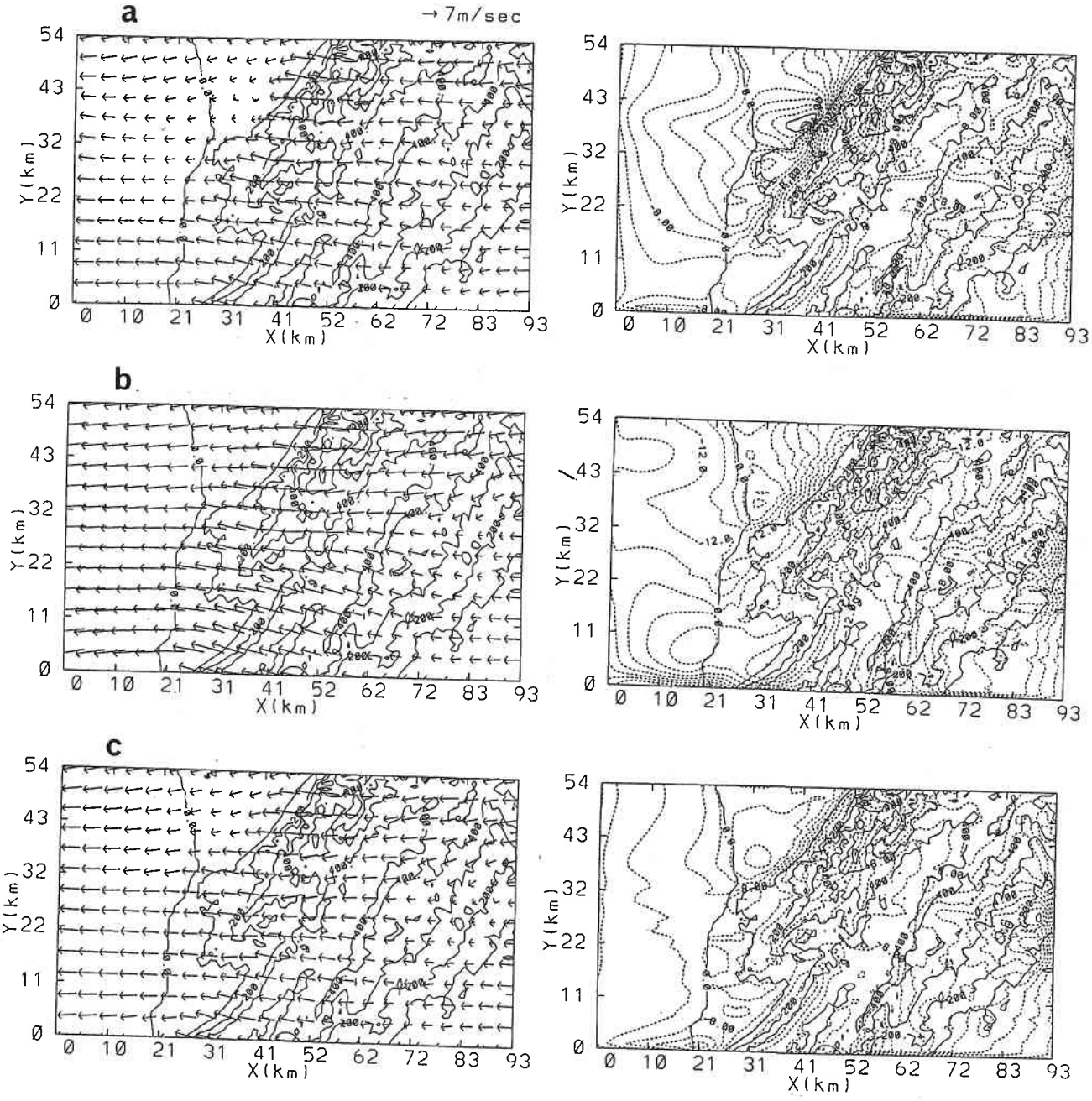

Wave breaking occurred in certain locations when a critical layer pre-existed in the upstream vertical wind profile, either with or without the upper westerly winds. It is concluded that the westerly wind in the upper layer is not a factor for generation of the downslope wind. The wave-overturning region appears to act as a reflector of the internal gravity waves and the wave resonance, established in the cavity between the ground and the reversal flow, results in the strong downslope winds on the lee slope. The strong shooting flow produced by the wave breaking appears analogous to hydraulic flow. The results show the importance of wave breaking and the wave resonant amplification mechanism to the development of the Adelaide gully wind. It was demonstrated that local secondary instability (KHI) occurred in the wave-breaking region, thus appearing to enhance the surface winds.

With no pre-existing critical layer in the upstream vertical wind profile, no wave breaking occurred. For these situations the Froude number

Fig. 11 As in Fig. 7 (a) and (b) but for the runs in the section on the influence of the critical layer.

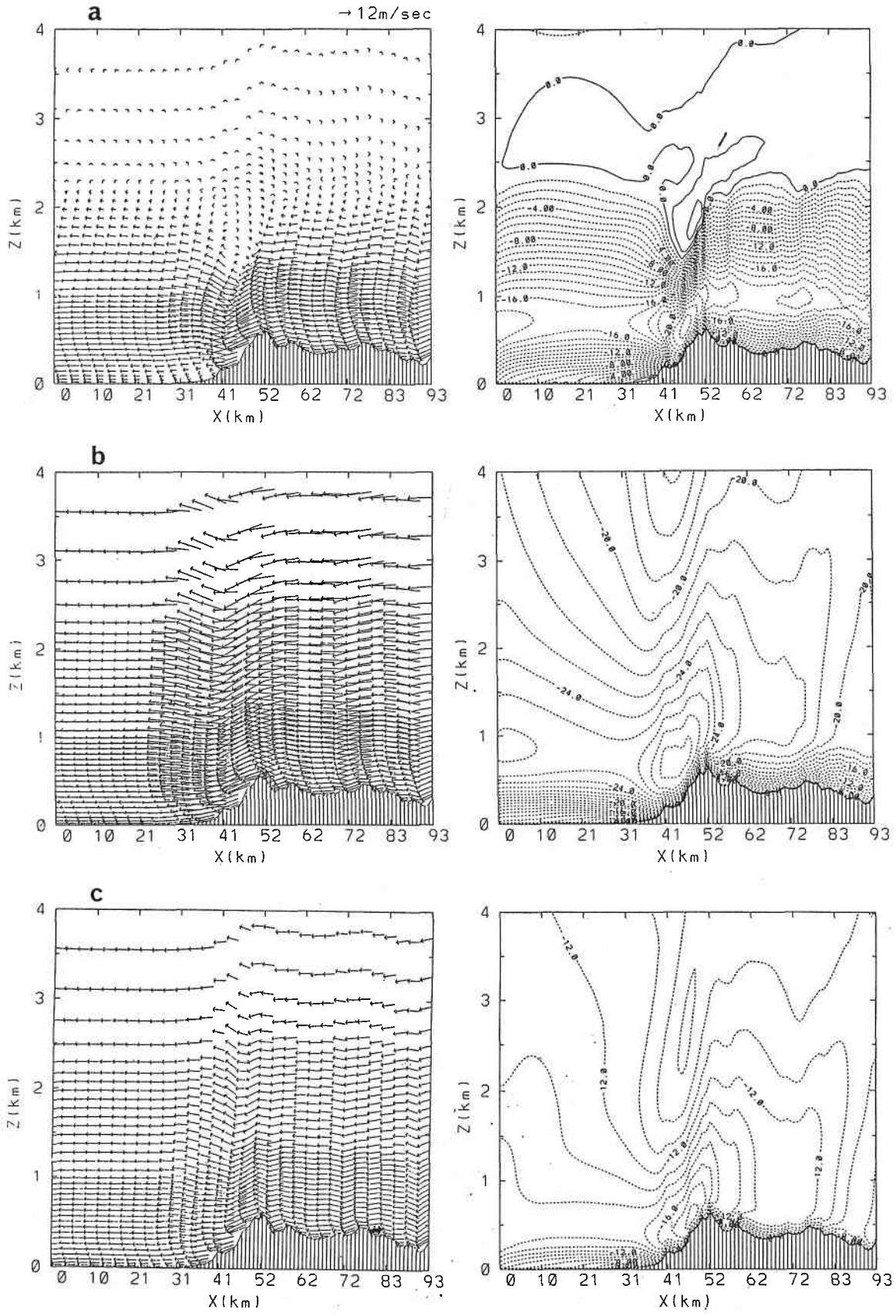

Fig. 12 As in Fig. 11 but for the potential temperature.

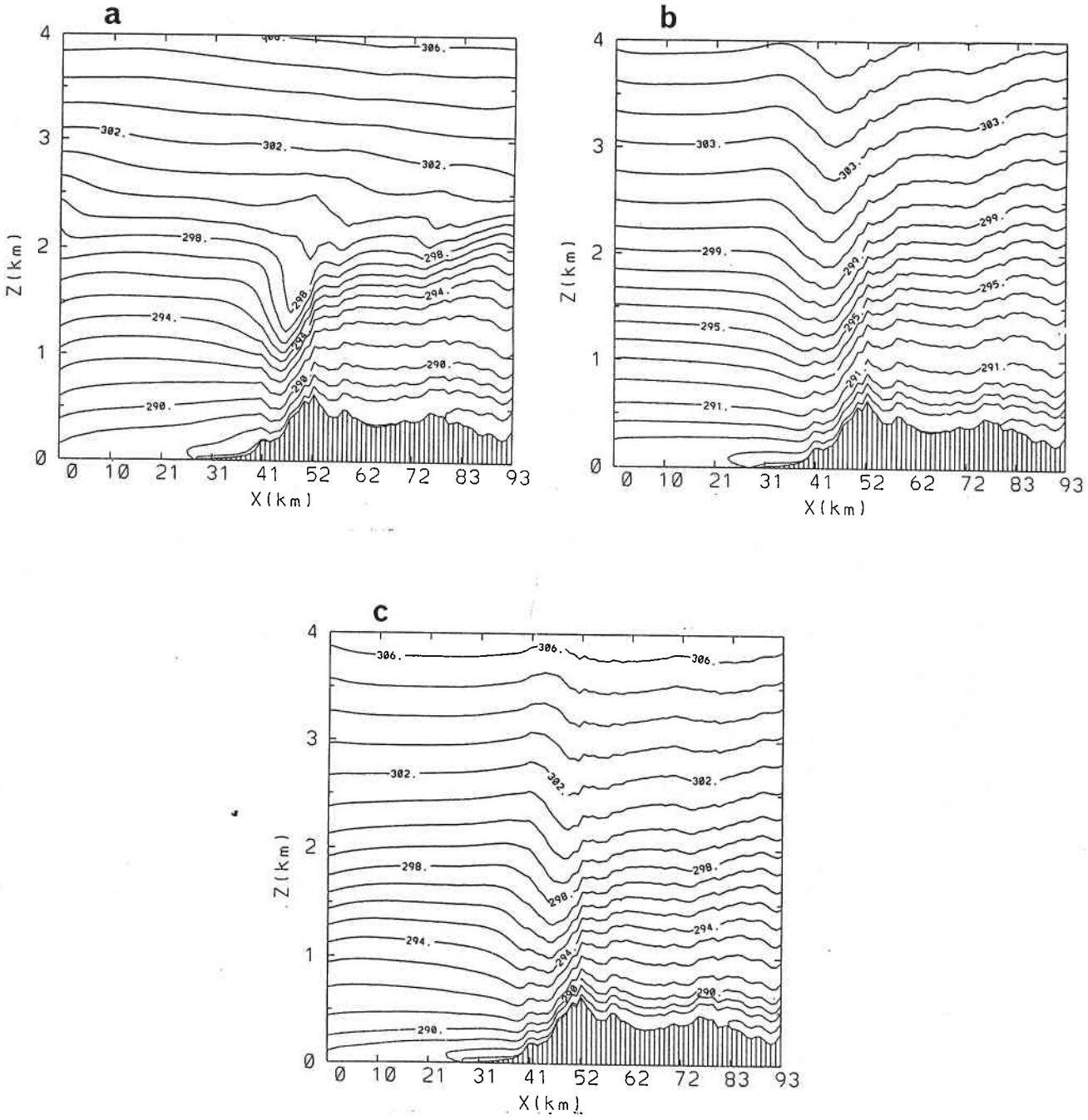

of the flow was less than the critical value required to produce the breaking. The wave structure was representative of the hydraulic flow dynamics. However, a moderately strong downslope wind was still produced by the transition to supercritical flow on the lee slope. These results are consistent with the hypothesis of the hydraulic amplification mechanism of the Adelaide gully wind (Grace and Holton 1990; Grace 1995). The numerical works of Durran (1986) also demonstrated that an inversion in the flow upstream of the Colorado Rockies can generate hydraulic-like shooting flows without wave breaking. The importance of the hydraulic amplification mechanism was demonstrated further by the experiments in which the resultant maximum wind speed decreased when the elevated inversion layer was removed. It is consistent with the suggestion

Fig. 13 As in Fig. 9 but for the runs in the section on the influence of the elevated inversion layer.

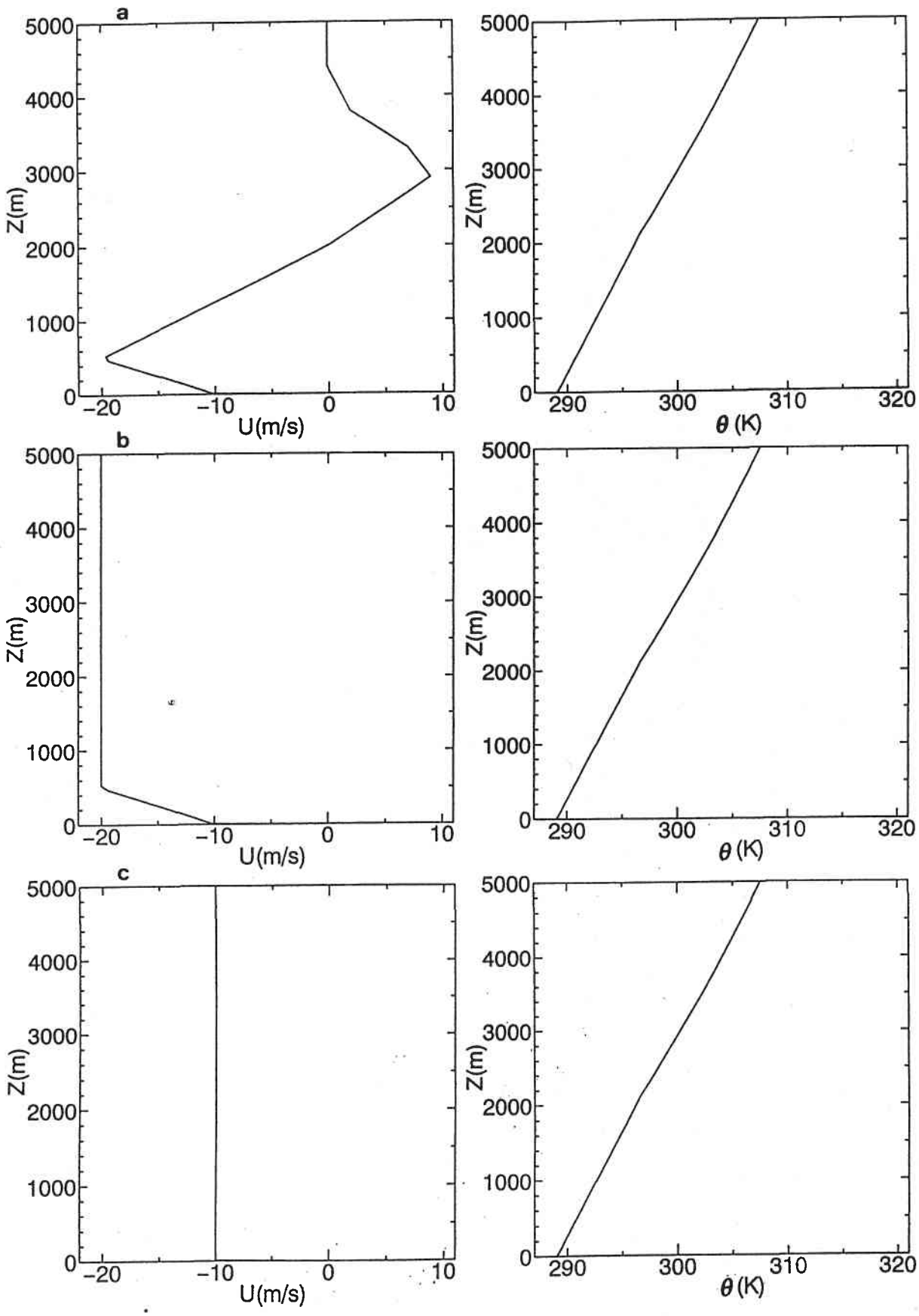

Fig. 14. As in Fig. 10 but for the runs in the section on the influence of the elevated inversion layer.

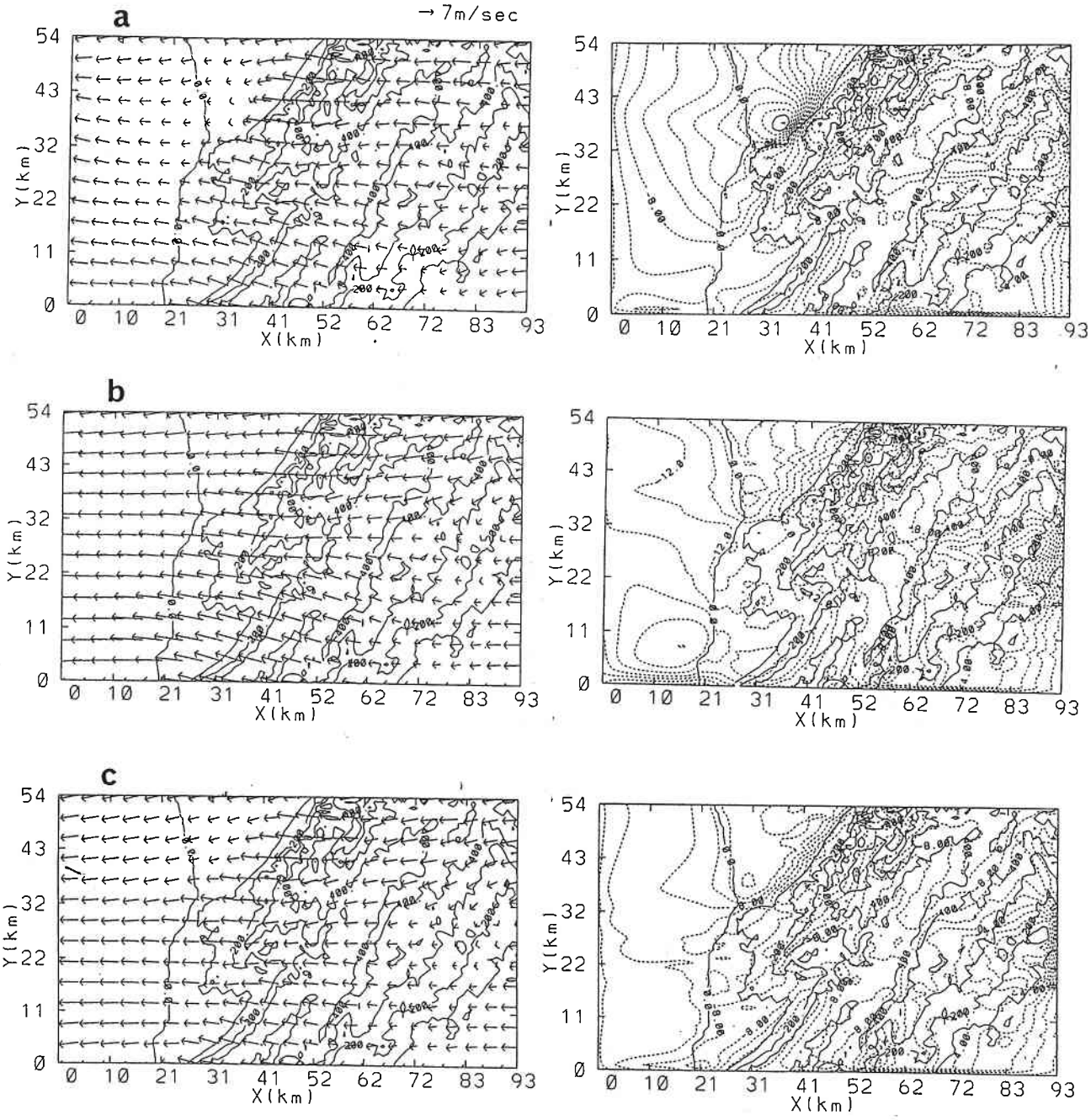

that the inversion may modulate the low-level flow structure when wave breaking does not occur beneath the inversion (Klemp and Durran 1987). It was also found that an elevated inversion layer is not an essential factor for the generation of the Adelaide gully wind when a pre-existing critical layer triggers wave overturning. The numerical result is consistent with Grace and Holton's (1988) finding that the presence of a subsidence inversion was poorly correlated with the occurrence of gully winds.

The numerical study suggests that the production of the Adelaide gully wind can be explained by either the wave resonant amplification mechanism or the hydraulic amplification mechanism. The shooting flows on the lee slope are fundamentally similar, but it is essential to consider both mechanisms when attempting to

Fig. 15 As in Fig. 11 but for the runs in the section on the influence of the elevated inversion layer.

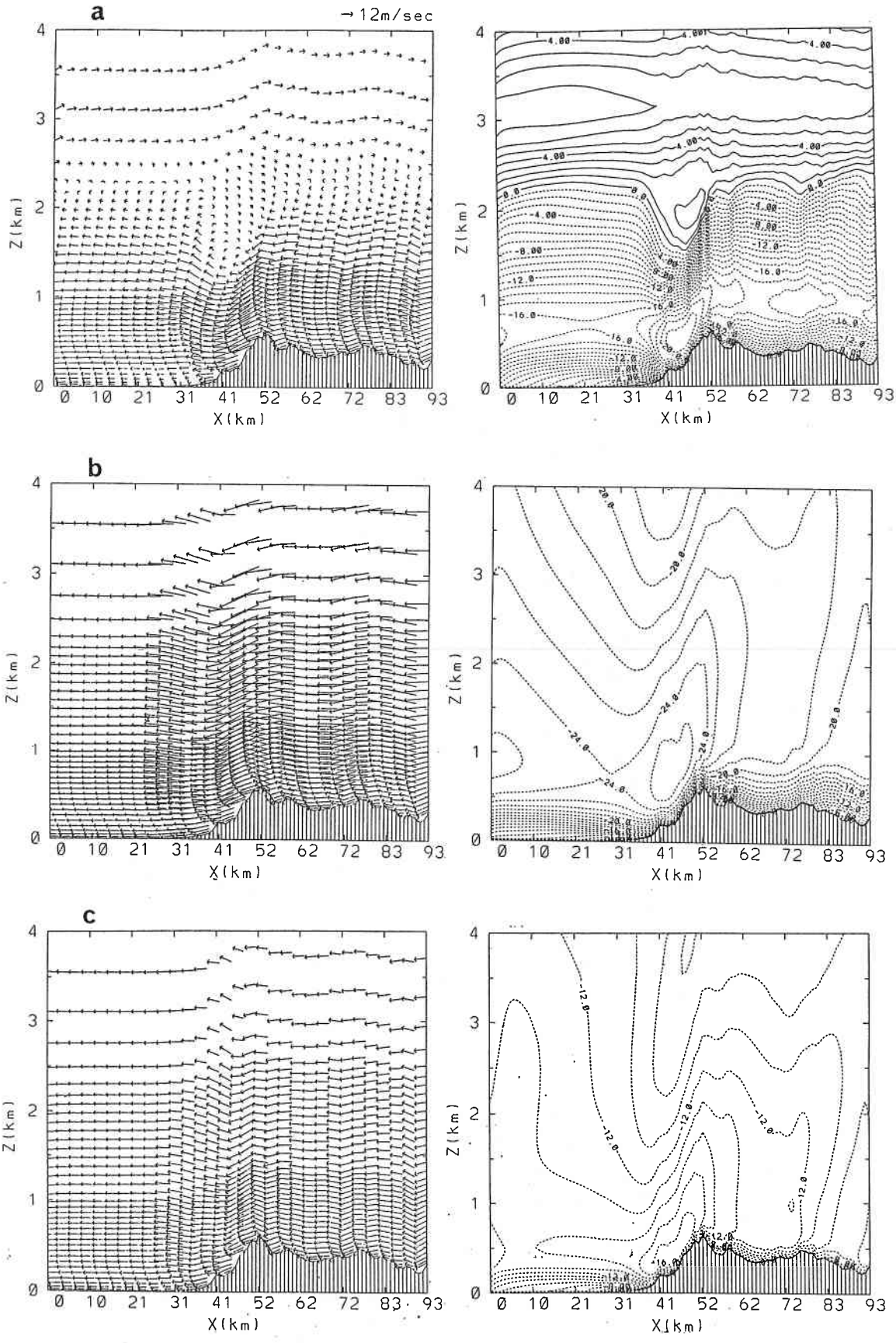

Fig. 16 As in Fig. 12 but for the runs in the section on the influence of the elevated inversion layer.

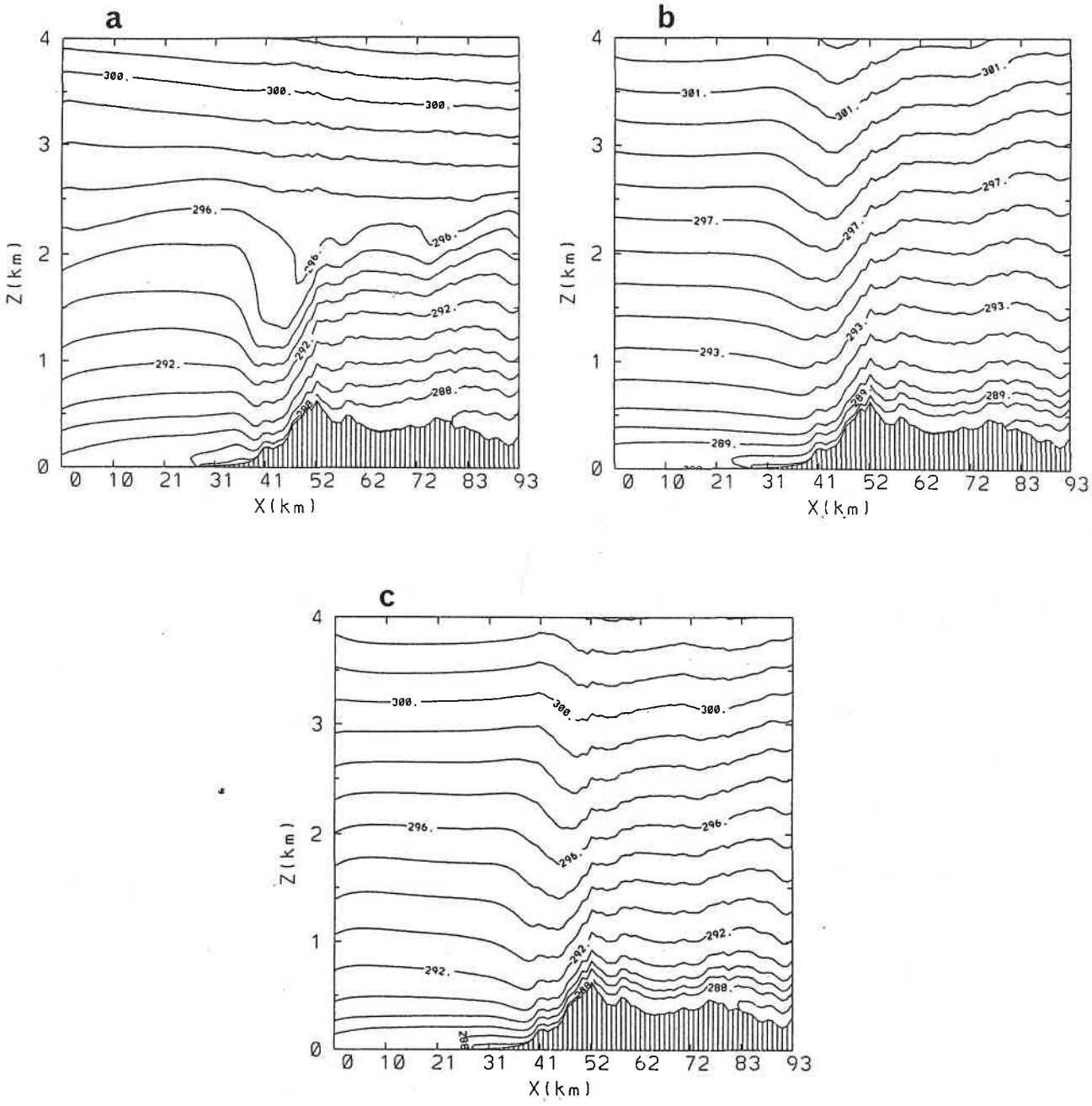

forecast this local wind. Although the pre-existing critical layer in the upstream wind profile is not a necessary or sufficient condition for the generation of strong winds along the lee slope, it is an important trigger for the Adelaide gully wind.

Although the model with a horizontal grid spacing $\Delta x = \Delta y = 2.5$ km can describe the local winds well, a sensitivity study showed that a grid size $\Delta x = \Delta y = 1$ km is desirable for resolving the fine structures of the Adelaide gully wind.

As Adelaide gully wind events occur mostly in the warmer months of the year and during the night, the effects of the local winds (e.g. the sea/land breezes and the cool drainage flow of the night) on this characteristic of the Adelaide gully wind are an aspect for further study. With the accumulation of a detailed observational dataset, it is expected that a numerical simulation will be done and this will further our understanding of the Adelaide gully winds.

Fig. 17 As in Fig. 6 but for the sensitivity run in the section on the sensitivity to horizontal grid spacing. The rectangles framed by solid lines are the domains in Fig. 6(a). Wind vectors and horizontal velocity u at surface (20 m). (b) As in (a) but for 440 m height.

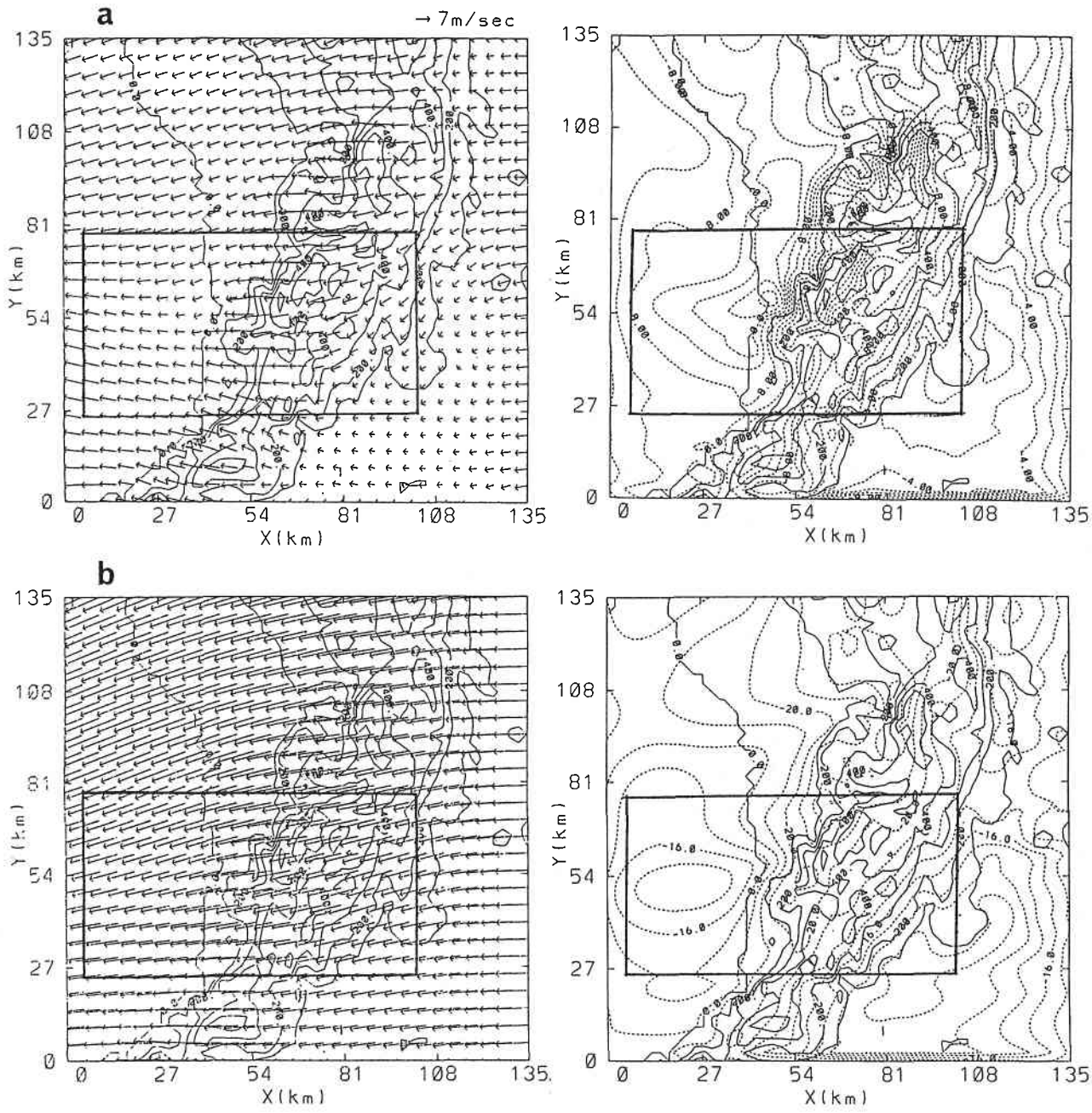

Acknowledgments

We are grateful to Dr P. Manins for his support and fruitful discussions. This work was conducted during the first author's stay at the Division of Atmospheric Research, CSIRO, Australia. The first author would like to thank Dr Roland A.D. Byron-Scott who invited him to visit the Flinders University of South Australia. Ian Holton's comments on a draft version were appreciated. Appreciation is also given to Prof. T. Miyazaki who supported the first author to finish this paper. Part of the computations were carried out at the computing center of National Institute for Environmental Studies, Japan.

Fig. 18 As in Fig. 7 but for the sensitivity run in the section on the sensitivity to horizontal grid spacing.

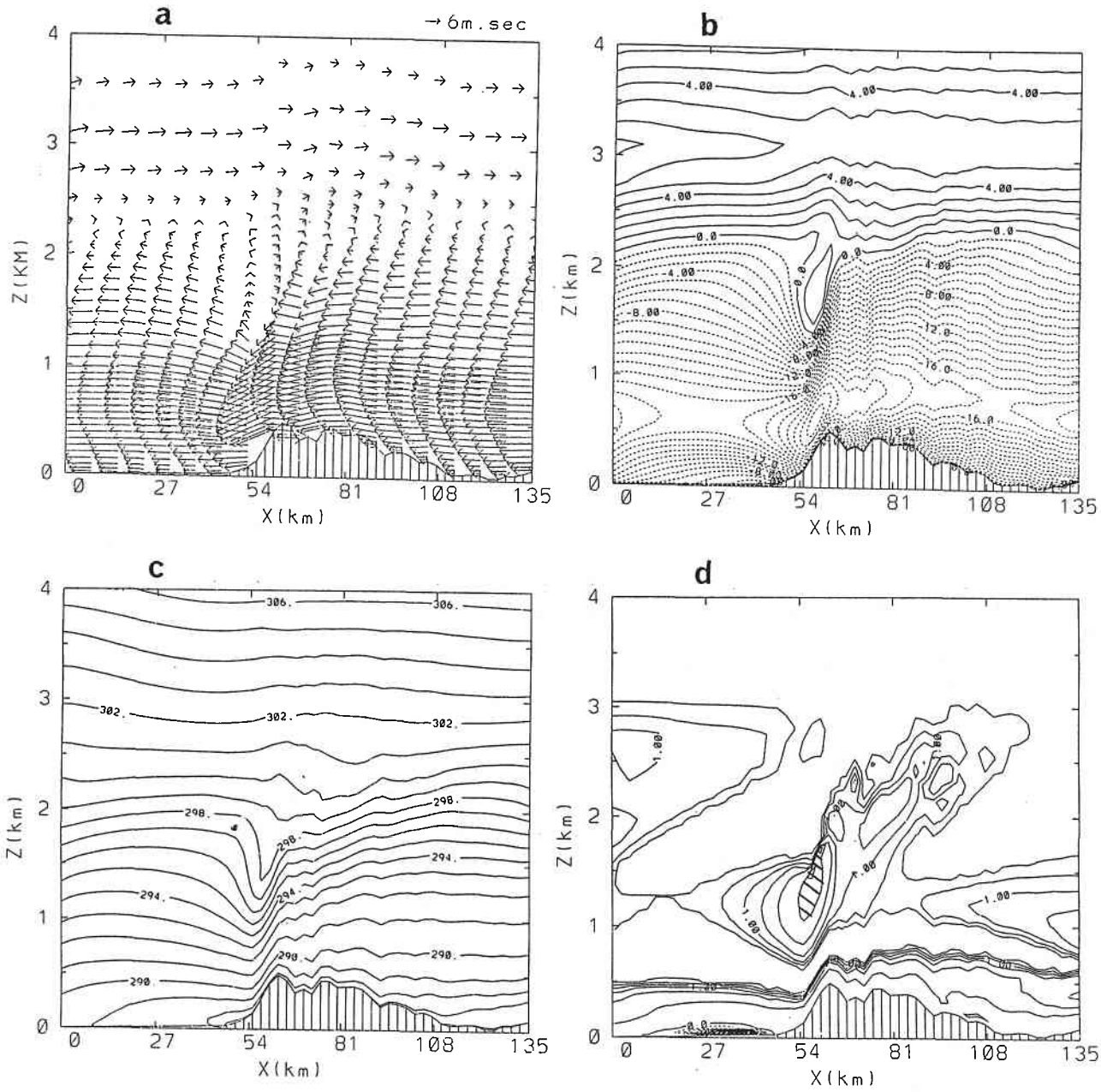

References

Akiyama, T. 1956. On the occurence of the local severe wind "Yamaji". Part 1. *J. Met. Res., 8*, 627–41.

Bacmeister, J.T. and Pierrehumbert, R.T. 1988. On high-drag states of nonlinear stratified flow over an obstacle. *J. Atmos. Sci., 45*, 63–80.

Bacmeister, J.T. and Schoeberl, M.R. 1989. Breakdown of vertically propagating two-dimensional gravity waves forced by orography. *J. Atmos. Sci., 46*, 2109–34.

Baines, P.G. and Hoinka, K.P. 1985. Stratified flow over two-dimensional topography in fluid of infinite depth: A laboratory simulation, *J. Atmos. Sci., 42*, 1614–30.

Baines, P.G. and Granek, J. 1990. Hydraulic models of deep stratified flows over topography. In L.J. Pratt (editor), *The Physical oceanography of Sea Straits*. Dordrecht: Kluwer, 245–69.

Blockley, J.A. and Lyons, T.J. 1994. Airflow over a two-dimensional escarpment. III: Nonhydrostatic flow. *Q. Jl R. met. Soc., 120*, 79–109

Bower, J.B. and Durran, D.R. 1986. A study of wind profile data collected upstream during windstorms in Boulder, Colorado. *Mon. Weath. Rev., 114*, 1491–1500.

Brinkman, W.A.R., 1974. Strong downslope winds at Boulder,

Colorado. *Mon. Weath. Rev., 102*, 592–602.

Castro, I.P. 1987. A note on the lee wave structure in stratified flow over three-dimensional obstacles. *Tellus, 39A*, 72–81.

Castro, I.P., Synder, W.H. and Marsh, G.L. 1983. Stratified flow over three-dimensional ridges. *J. Fluid Mech., 135*, 261–82.

Clark, T.L. and Peltier, W.R. 1977. On the evolution and stability of finite amplitude mountain waves. *J. Atmos. Sci., 34*, 1715–30.

Clark. T.L. and Peltier, W.R. 1984. Critical level reflection and the resonant growth of nonlinear mountain waves. *J. Atmos. Sci., 41*, 3122–34.

Clark, T.L. and Farley, R.D. 1984. Severe downslope windstorm calculations in two and three dimensions using anelastic interactive grid nesting: A possible mechanism for gustiness. *J. Atmos. Sci., 41*, 329–50.

Durran, D.R. 1986. Another look at downslope windstorms. Part I: The development of analogs to supercritical flow in an infinitely deep, continuously stratified flow. *J. Atmos. Sci., 43*, 2527–43.

Durran, D.R. 1990. Atmospheric processes over complex terrain. *Meteorological Monographs, 23*, 59–81.

Durran, D.R. and Klemp, J.B. 1983. A compressible model for the simulation of moist mountain waves. *Mon. Weath. Rev., 111*, 2341–61.

Durran, D.R. and Klemp, J.B. 1987. Another look at downslope winds. Part II. Nonlinear amplification beneath wave-overturning layers. *J. Atmos. Sci.,44*, 3402–12.

Grace, W. 1992. Downslope winds. PhD thesis, Flinders University of South Australia, 112pp.

Grace, W. 1995. Downslope wind. *Met. Study 41*, AGPS, Canberra, 83 pp.

Grace, W. and Holton, I. 1988. A mechanism for downslope winds with special reference to the Adelaide Gully Wind. *Met. Note 179*, Bur. Met., Australia, 35pp.

Grace, W. and Holton, I. 1990. Hydraulic jump signatures-associated with Adelaide downslope winds. *Aust. Met. Mag., 38*, 43–52.

Gross, G. 1987. Some effects of deforestation on nocturnal drainage flow and local climate-A numerical study. *Bound. Lay. Met., 38*, 37.

Hoinka, K.P. 1985a. Observation of the airflow over the Alps during a foehn event. *Q. Jl R. met. Soc., 111*, 192–224.

Hoinka, K.P. 1985b. A comparison of numerical simulations of hydrostatic flows over mountains with observations. *Mon. Weath. Rev., 113*, 719–35.

Holton, I.C. 1985. The Adelaide gully wind and associated hazards to aviation. *Met. Note 166*, Bur. Met., Australia.

Holton, I.C. and Grace, W. 1989a. The Adelaide downslope winds. Part I: Nowcasting turbulence and wind shear. *Met. Note 186*, Bur. Met., Australia.

Holton, I.C. and Grace, W. 1989b. The Adelaide downslope winds. Part II: Nowcasting wind speed. *Met. Note 189*, Bur. Met., Australia.

Ikawa, M. 1990. High-drag states and Foehns of a two-layered stratified fluid past a two-dimensional mountain. *J. met. Soc. Japan, 68*, 163–82.

Ikawa, M., and Nagasawa, Y. 1989. A numerical study of a dynamically induced foehn observed in the Abashiri-Ohmu area. *J. met. Soc. Japan, 67*, 429–58

Klemp, J.B. and Lilly, D.K. 1975. The dynamics of wave-induced downslope winds. *J. Atmos. Sci., 32*, 320–39.

Klemp, J.B. and Lilly, D.K. 1978. Numerical simulation of hydrostatic mountain waves. *J. Atmos. Sci., 35*, 78–107.

Klemp, J.B. and Durran D.R. 1987. Numerical modeling of Bora winds. *Met. Atmos. Phys., 36*, 215–27.

Küttner, J. 1939. Moazagotl und Föhnwelle. *Beitr. Phys. frei. Atmos., 25*, 79–114.

Laprise, R. and Peltier, W.R. 1989. The structure and energetics of transient eddies in a numerical simulation of breaking mountain waves. *J. Atmos. Sci., 46*, 565–85.

Lilly, D.K. and Zipser, E.J. 1972. The front range windstorm of 11 January 1972–A meteorological narrative. *Weatherwise, 25*, 56–63.

Lilly, D.K. and Klemp, J.B. 1979. The effects of terrain shape on nonlinear hydrostatic mountain waves. *J. Fluid Mech., 95*, 241–61.

Long, R.R. 1954. Some aspects of the flow of stratified fluids II, Experiments with a two fluid system. *Tellus, 6*, 97–115.

Mahrer, Y. and Pielke, R.A. 1977. The effects of topography on sea and land breezes in a two-dimensional numerical model. *Mon. Weath. Rev., 105*, 1151–62.

Marsh, L. 1987. Towards an understanding of the Adelaide gully wind. *Met. Note 175*, Bur. Met., Australia, 37pp.

Miller, P.P. and Durran, D.R. 1991. On the sensitivity of downslope windstorms to the asymmetry of the mountain profile. *J. Atmos. Sci., 48*, 1457–73.

Miranda, P.M.A. and James, I.N. 1992. Non-linear three-dimensional effects on gravity-wave drag: splitting flow and breaking waves. *Q. Jl R. met. Soc., 118*, 1057–81.

Neiman, P.J., Hardesty, R.M., Shapiro, M.A. and Cupp, R.E. 1988. Doppler lidar observation of a downslope Sandstorm. *Mon. Weath. Rev., 116*, 2265–75.

Peltier, W.R. and Clark, T.L. 1979. The evolution and stability of finite-amplitude mountain waves. Part II: Surface wave drag and severe downslope windstorms. *J. Atmos. Sci.,36*, 1498–1529.

Peltier, W.R. and Scinocca, J.F. 1990. The origin of severe downslope windstorm pulsations. *J. Atmos. Sci., 47*, 2853–70.

Physick, W.L. 1988. Mesoscale modeling of a cold front and its interaction with a diurnally heated land mass. *J. Atmos. Sci., 45*, 3169–87.

Pielke, R.A. 1974a. A three-dimensional numerical model of the sea breeze over South Florida. *Mon. Weath. Rev., 102*, 115–39.

Pielke, R.A. 1974b. A comparison of the three-dimensional and two-dimensional numerical predictions of the sea breezes. *J. Atmos. Sci., 31*, 1577–85.

Pitts, R.O. and Lyons, T.J. 1989. Airflow over a two-dimensional escarpment. I: Observations. *Q. Jl R. met. Soc., 115*, 965–81.

Pitts, R.O. and Lyons, T.J. 1990. Airflow over a two-dimensional escarpment. II: Hydrostatic flow. *Q. Jl R. met. Soc., 116*, 363–78.

Richard, E., Mascart, P. and Nickerson, E.C. 1989. On the role of the surface friction in downslope windstorms. *Jnl appl. Met., 28*, 241–51.

Rottman, J.W. and Smith, R.B. 1989. A laboratory model of severe downslope winds. *Tellus, 41A*, 401–15.

Saito, K., 1993. A numerical study of the local downslope wind "Yanaji-Kaze" in Japan. Part 2. Non-linear aspect of the 3-D flow over a mountain range with a col. *J. met. Soc. Japan, 71*, 247–70.

Saito, K. and Ikawa, M. 1991. A numerical study of the local downslope wind "Yanaji-Kaze" in Japan. *J. met. Soc. Japan, 69*, 31–56.

Schumann, U. and Volkert, H. 1984. Three-dimensional mass- and momentum-consistent Helmholtz equation in terrain-following coordinates. In: W. Hackbush (ed), Efficient solutions of elliptic sytems, Proc. GAMM-Seminar, Kiel, 27–29 Jan. 1984, *Notes on numerical Fluid Mechanics. Vol: 10*, Vieweg, Brannschweig.

Scinocca, J.F. and Peltier, W.R. 1989. Pulsating downslope windstorms. *J Atmos. Sci., 46*, 2885–914.

Scinocca, J.F. and Peltier, W.R. 1991. On the Richardson number dependence of nonlinear critical-layer flow over localized topography. *J. Atmos. Sci., 48*, 1560-72.

Scinocca, J.F. and Peltier, W.R. 1993. The instability of Long's stationary solution and the evolution towards severe downslope-windstorm flow. Part I: Nonlinear numerical simulation. *J. Atmos. Sci., 50*, 2245–63.

Scinocca, J.F. and Peltier, W.R. 1994. The instability of Long's